JJEE

Volume 12 | Number 3 | September 2026 | Pages 483-504

Jordan Journal of Electrical Engineering

ISSN (print): 2409-9600, ISSN (online): 2409-9619

Homepage: jjee.ttu.edu.jo

Unified Intelligent Fault Location Protocol For Active Distribution Grid

Nadir Mohamed[1], Md Shafiullah[2, 3], Md Reyaz Hussan[3*]

[1] Electrical Engineering Department, King Fahd University of Petroleum & Minerals, Dhahran 31261, Saudi Arabia

[2] Control and Instrumentation Engineering Department, King Fahd University of Petroleum & Minerals, Dhahran 31261, Saudi Arabia

[3] IRC for Sustainable Energy Systems, King Fahd University of Petroleum & Minerals, Dhahran 31261, Saudi Arabia

E-mail: mohammad.hussan@kfupm.edu.sa

Received: Dec 16, 2025 *Revised: Mar 26, 2026* *Accepted: May 16, 2026* *Available online: Aug 15, 2026*

***Abstract*—** In this paper, a single fault-diagnosis framework of electrical systems operating under non-stationary conditions is proposed. The algorithm is a hybrid of spectral analysis with Short-Time Fourier Transform (STFT) and adaptive time-frequency analysis with Hilbert-Huang Transform (HHT) to obtain complimentary fault-relevant features. They are combined features which are fed to a trained neural-network classifier in a coordinated learning protocol. In contrast to traditional methods that use discrete signal-processing or learning methods, the suggested framework incorporates multi-resolution time-frequency representation into a hierarchical diagnostic process. The method is more sensitive to non-persistent and non-stationary faults and is also more robust to classification. The effectiveness of the proposed unified protocol to provide accurate and reliable fault identification is confirmed through the validation of its effectiveness through extensive simulation.

***Keywords*—** Active distribution grid; Power distributed network; Fault location; Machine learning model; Renewable energy.

1. INTRODUCTION

The electric power system integrates generation, transmission, and distribution to deliver electricity to end users. Within this system, the distribution network forms the link between the supplier and the consumer. Its primary duty is to provide customers with electrical energy that is both high quality and highly reliable [1, 2]. However, distribution networks are prone to faults that disrupt operation and trigger power outages, adversely affecting customers in the impacted area and leading to significant economic losses. According to [3], faults in distribution networks account for more than 80% of power outages. The challenge is compounded by uncertainty in the fault's location and type, which complicates troubleshooting and raises repair costs because crews must first diagnose the fault before implementing the appropriate fix [4, 5]. Therefore, rapid and reliable methods for fault detection, classification, and location are essential to streamline grid maintenance. Accurate detection allows operators to isolate the faulted section from the healthy network, ensuring that only the affected area experiences an interruption while service to unaffected customers is maintained [6].

Moreover, an effective classification step ensures the appropriate corrective action is taken. The identified fault type provides actionable insights that guide maintenance crews to

* Corresponding author

DOI: https://doi.org/10.5455/jjee.204-1765873163

the right repair, enabling faster service restoration. As a result, the adverse impacts, outage duration, and associated revenue losses are reduced [7, 8]. Substantial R&D has targeted improving fault diagnosis in distribution networks. At the same time, the penetration of distributed generation (DG)—drawing on both renewable and conventional sources and often coupled with energy storage—has surged because of its techno-economic benefits, such as reducing transmission losses, lowering greenhouse-gas emissions, and supporting reactive power. Yet the presence of DG alters network behavior and renders many traditional fault-diagnosis approaches less effective [9, 10, 11]. In addition, the variability and intermittency of solar and wind generation further complicate fault-diagnosis methods and erode their effectiveness. Consequently, conventional protection and diagnostic schemes must be substantially upgraded to accommodate the growing penetration of distributed generation in electric grids [12, 13].

Methods for addressing failures in distribution networks are commonly grouped into three classes: traveling-wave, impedance-based, and knowledge-based techniques. In the traveling-wave approach, the transient waves that propagate between a line terminal and the fault point are analyzed—using their transmission and reflections—to infer fault characteristics and location [14]. Fault information for long distances may be correctly provided by the travelling wave-based approaches through the transmission lines [4]. However, the inherent properties of distribution feeders severely degrade the accuracy of traveling-wave schemes, and deploying them on distribution networks is relatively costly [15]. By contrast, impedance-based techniques became far more popular than traveling-wave methods because they are simpler to implement and less costly to operate.

Nevertheless, in DG-rich networks the accuracy of impedance-based schemes degrades due to parameter-estimation errors, the influence of fault resistance, and the presence of multiple laterals [16]. Conversely, the third class—knowledge-based methods—overcomes the multiple-estimation issue by leveraging machine-learning techniques to deliver insightful, cost-effective solutions [17, 18]. Recently, signal-processing methods have been paired with knowledge-based approaches to detect power-quality disturbances (PQDs). Representative techniques include the wavelet transform [19], Hilbert–Huang transform [20], Kalman filtering [21], and the Stockwell transform [22]. Signal-processing tools have also been applied to power-system fault diagnosis. For instance, [23] proposed a signal-processing–driven neural-network classifier whose parameters were optimized via a genetic algorithm; however, the study did not assess how loading uncertainty affects performance. In [24- 26], the S-transform combined with artificial neural networks achieved effective fault identification and classification with satisfactory accuracy. Additionally, [27] trained and tested a convolutional neural network on time–frequency energy matrices of fault signals, but did not address fault localization.

Furthermore, most of the aforementioned methods overlook the adverse effects and uncertainties introduced by integrating renewable energy resources into distribution grids. Only a few recent studies accounts for such integration, namely impedance-based [28], heuristic [29], intelligent [30], and voltage-sag–based [31] schemes, but these typically omit real-time simulation of the distribution network, leaving their practical effectiveness uncertain. Consequently, many existing diagnostic approaches fail to address the key challenges of active distribution feeders. To bridge this gap, this paper presents a unified, fault-type–agnostic fault-location protocol for active distribution feeders that also performs fault detection and classification. Although there has been a great advancement in signal-processing- and neural-network-based fault-diagnosis, the current methods usually utilize either fixed time-frequency analysis methods or independent learning models without a cohesive framework. Most approaches are based on one representation, which limits them to robustness to non-stationary operating conditions, whereas others are not systematic in integrating feature extraction and classification phases. Specifically, coordinated localization of spectral and adaptive decomposition in STFT and HHT are hardly used in a coordinated diagnostic protocol due to the complementary nature of their capabilities. To overcome these shortcomings the paper suggests the integrated fault-diagnosis system based on the combination of multi-resolution STFT and HHT feature-extraction and the organized neural-network-based learning scheme. The suggested protocol offers systematic and scalable pipeline to trustful fault detection in and through the fluctuating and temporary operating conditions. The principal contributions are as follows:

- Modeling an active distribution feeder incorporating the intermittency of the solar PV generation and load demand.
- Development of intelligent strategies by combining signal processing tools and machine learning models for fault diagnosis under fault information uncertainty.
- Developing a reliable fault localization model independent of the fault type and capable of accurately pinpointing faults without prior classification.
- Validation of the developed models through comparison and evaluation of performance metrics.

The rest of the article is organized as follows: Section 2 presents the active distribution model configurations, while Section 3 demonstrates the methodology, including the unified fault location strategy. Section 4 presents the results and discussions, and the concluding remarks are presented in Section 5.

2. ACTIVE DISTRIBUTION GRID MODEL

Firstly, the overall workflow is outlined in Fig. 1. The test network in Fig. 2 includes a 60 Hz feeder, two power transformers, a distribution line, a solar PV farm, and a lumped load. The system is modeled in MATLAB/Simulink using the Simscape Electrical Toolbox libraries (motors, loads, power sources, transformers, overhead lines, and underground cables). After assembling the components, the “discrete” option in the “PSB option menu” is selected with a sampling time of 0.00005 s, yielding a 20 kHz rate (≈333 samples per cycle). In this work, in order to represent faults at different locations, the distribution line is divided into two segments of lengths ‘a1’ and ‘a2’, with a1+ a2 =12 km, representing the entire distribution line. The three-phase load active power (P) is set to 1.0, 1.2, and 1.25 MW, and the reactive power (Q) to 0.48, 0.50, and 0.52 MW, with a 5% load variation applied. Fault resistance is randomly selected up to 15 Ω. A solar PV farm acts as the feeder (the renewable source in the model), with specifications provided in Table 1.

3. METHODOLOGIES

Advances in computing power over the 20th century enabled widespread use of signal-processing methods that had been constrained in the 19th century by limited computational resources [32]. These techniques yield richer representations of power-system signals and a more complete characterization of system behavior. Examples include the Fourier transform, Stockwell transform, wavelet transform, Hilbert–Huang transform (HHT), and short-time Fourier transform (STFT). In parallel, machine-learning methods have shown strong performance across many domains, enabling computers to perform tasks akin to human decision-making [33]. Combining machine learning with signal processing is therefore highly promising for power-system applications. In this study, STFT and HHT, with associated statistical indices are used for feature extraction, and the resulting features are supplied to feed-forward neural networks (FFNNs) trained to detect, classify, and locate faults in a simulated active distribution network.

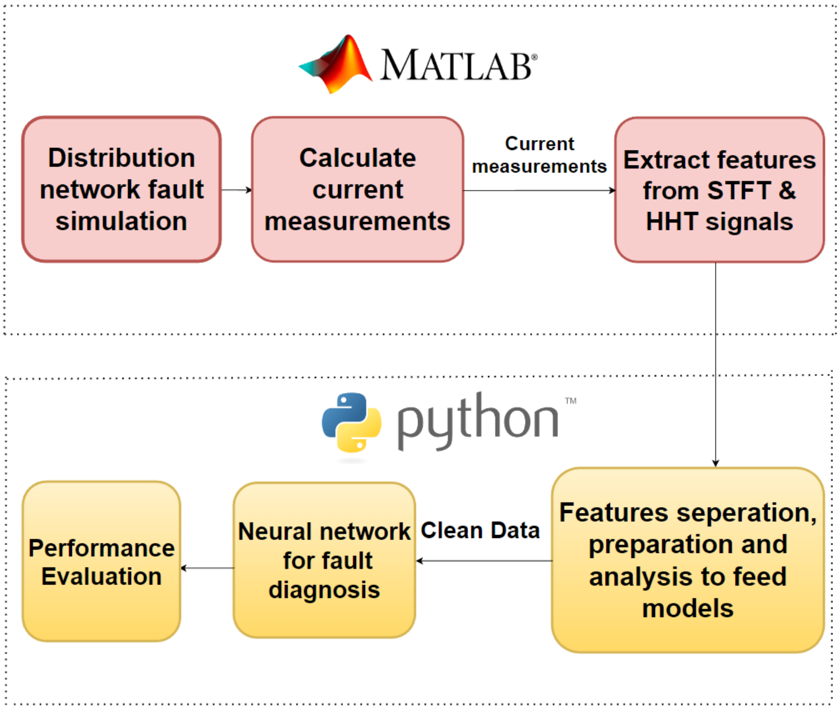

Fig. 1. Block diagram showing full protocol's procedure.

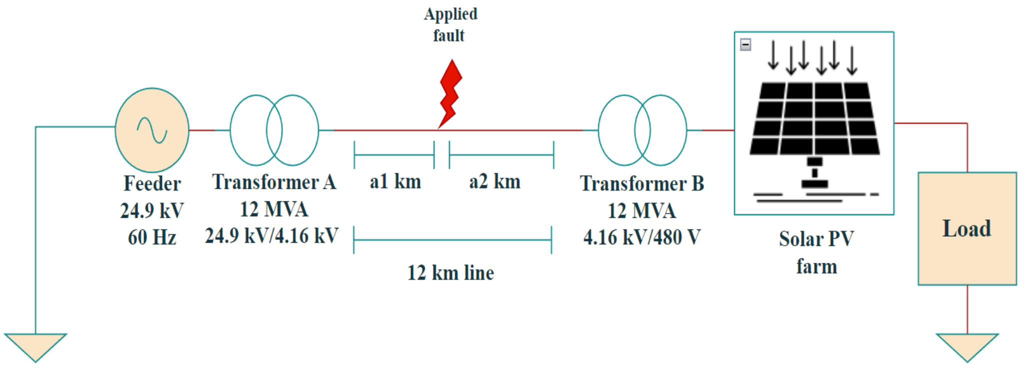

Fig. 2. The distribution network model.

Table 1. Solar PV farm specifications

Quantity	Value
Voltage	480 V
Phase angle	0°
Rated power	0.25 MW
Reactive power	50 kVAR
Actual power delivered	60% to 100% of the rated value

3.1. Short-time Fourier Transform (STFT)

The Fourier transform (FT) is a fundamental tool for representing and analyzing signals in the frequency domain. For a continuous-time signal x(t), it is defined as:

$$X(\omega) = \int_{-\infty}^{\infty} x(t)e^{-j\omega t}\,dt \quad (1)$$

where, $X(\omega)$ is the FT pair of the signal $x(t)$, represented in the frequency domain.

A limitation of the FT is that it reveals only the overall frequency content of a signal, offering no insight into when specific disturbances occur, since it averages over the entire time record. To address this, time frequency analysis techniques such as the short-time Fourier transform (STFT) were introduced [34], [35]. STFT is well suited to extracting fault-related information in power systems. It computes a sequence of Fourier transforms on windowed segments of the signal (windowing in time corresponds to convolution in frequency), yielding frequency information that is localized in time when the signal's spectral content varies, unlike the conventional FT, which provides only a time-averaged spectrum [34]. The STFT of a signal can be computed by the following equations [34, 36]:

$$STFT\,\{x(t)\} = X(\tau,\omega) = \int_{-\infty}^{\infty} x(t)\,h(t-\tau)e^{-j\omega t}\,dt \quad (2)$$

The STFT of a signal can be obtained by modulating a signal $x(t)$ by $e^{-j\omega t}$, then passing it through a filter with the impulse response of $h(t)$. In addition, it can also be considered as the FT of $\{x(t)\,h(t-\tau)\}$, which is a convolution in the frequency domain. Moreover, the discrete version of STFT is defined as follows:

$$X_{STFT}[m,n] = \sum_{k=0}^{L-1} x[k]\,h[k-m]e^{-j2\pi nk/L} \quad (3)$$

$$x[k] = \sum_m \sum_n X_{STFT}[m,n]\,h[k-m]e^{j2\pi nk/L} \quad (4)$$

where, $x[k]$ is the signal of interest, while $\mathrm{h(k-m)}$ is an L-point windowing function. Also, m and n are the discrete variables of the STFT signal in the frequency domain.

In the STFT, there is an inherent time–frequency trade-off, a short (narrow) window yields fine temporal resolution but coarse spectral resolution, whereas a long (wide) window improves frequency resolution at the expense of timing precision. The STFT is commonly visualized with a spectrogram, an intensity map of the transform magnitude over time and frequency [34].

3.2. Hilbert Huang transform

The first signal-processing method used in this study is the Hilbert–Huang transform (HHT), which combines empirical mode decomposition (EMD) with the Hilbert transform (HT). EMD decomposes the measured signal into intrinsic mode functions (IMFs). Applying the HT to each IMF produces the instantaneous amplitude (IA) and instantaneous frequency (IF) components [37, 38, 39]. The following subsections detail the steps of the HHT procedure.

3.2.1. The Empirical Mode Decomposition

Huang [37] initially describes empirical mode decomposition (EMD) as decomposing a particular signal into a limited number of IMFs. Each oscillation mode that the signal can experience is represented by an IMF, which meets the following conditions:

- The numbers of zero crossings and extrema should be the same, or differ by no more than one.

- The mean of the upper (maxima) and lower (minima) envelopes is zero, i.e., their local average vanishes at every point.

The stages involved in the filtering process, which is used to obtain IMFs from a signal $x(t)$, are as follows [37]:

- Step #1: The upper envelope is formed by connecting the signal's local maxima with a cubic-spline interpolation.
- Step #2: The lower envelope is built by similarly connecting the local minima.
- Step #3: Calculating the mean m_1 of the upper and lower envelopes.
- Step #4: Subtracting the local mean m_1, the average of the upper and lower envelopes, from the original signal $x(t)$ yields the first component or proto-IMF (h_1).

$$h_1 = x(t) - m_1 \tag{5}$$

- Step #5: If h_1 meets specific requirements, the filtering process is completed, and h_1 becomes the first IMF. If not, repeat steps 1 through 4 on h_1 and successive signals until a component h_{1k} is obtained that satisfies the requirements.

$$h_{1k} = h_{1(k-1)} - m_{1k} \tag{6}$$

It is then written as:

$$u_1(t) = h_{1k} \tag{7}$$

where $u_1(t)$ represents the first IMF of $x(t)$. The first residue $r_1(t)$ of $x(t)$ is determined as follows:

$$r_1(t) = x(t) - u_1(t) \tag{8}$$

- Step # 6: To find the second IMF, $u_2(t)$, and so on; steps 1 through 5 are executed again on the received signal $x(t)$. When a residue $r_n(t)$ falls below a threshold value or turns monotonic, the EMD process is terminated. The final representation of a signal after it has been thoroughly deconstructed is:

$$\sum_{j=1}^{n} u_j + r_n \tag{9}$$

3.2.2. The HT Methodology

The HT is a phase shifter for continuous time signal u(t). What this tool does is it shifts its input signal $u(t)$ using the following equation:

$$\hat{u}(t) = \frac{1}{\pi}\int_{-\infty}^{+\infty} \frac{u(\alpha)}{(t-\alpha)} d\alpha \tag{10}$$

where, $\hat{u}(t)$ is the Hilbert transform of signal u(t). Also, $\hat{u}(t)$ can be expressed as:

$$\hat{u}(t) = u(t) * \left(\frac{1}{\pi t}\right) \tag{11}$$

where, * represents the convolution operation. So, the HT of a signal u(t) is the convolution of the signal itself with $\frac{1}{\pi t}$. The HT produces a signal $y(t)$ that has the following representation:

$$y(t) = u(t) + j\,\hat{u}(t) = A(t)e^{j\theta(t)} \tag{12}$$

where, $A(t)$ and $\theta(t)$ are the IA and the instantaneous phase, respectively. $A(t)$ and $\theta(t)$ can be expressed as follows:

$$A(t) = [u^2(t) + \hat{u}^2(t)]^{1/2} \tag{13}$$

$$\theta(t) = \tan^{-1}\left(\frac{\hat{u}(t)}{u(t)}\right) \tag{14}$$

The instantaneous frequency is known to the derivative of the phase with respect to time as follows:

$$f(t) = \frac{1}{2\pi}\frac{d\theta}{dt} \tag{15}$$

EMD is a data-adaptive method that decomposes a signal based on its time-domain characteristics, making it well suited for analyzing nonlinear and nonstationary data. Because the resulting IMFs are mono-component oscillatory modes, deriving instantaneous frequency (IF) from them yields quantities with clear physical meaning.

3.3. Artificial Neural Networks

Artificial intelligence (AI) describes machines' capacity to learn and pursue predefined goals, emulating human cognitive problem-solving. Among AI techniques, artificial neural networks (ANNs) are especially prominent, inspired by biological neural circuitry. The simplest form is the feed-forward neural network (FFNN), trained in a supervised manner to learn input–output mappings for classification and regression. An FFNN comprises input, hidden, and output layers built from perceptrons. Nodes in successive layers are connected by weights; each node sums its weighted inputs with a bias and applies a nonlinear activation, passing the result forward layer by layer until the output is produced [38]. Training typically begins with randomly initialized weights; predictions are computed, errors relative to targets are measured, and the weights are iteratively updated until an adequate fit is reached [40-42]. Optimization methods (solvers) such as Adam and stochastic gradient descent are commonly used—with backpropagation providing gradients—to tune model parameters. Typical activation (squashing) functions include ReLU, logistic/sigmoid, tanh, and softmax [22].

3.4. Fault Diagnosis Strategy

This section details the proposed framework shown in Fig. 3, including the simulated test network, the feature-extraction pipeline, and the ANN-based modules for fault detection, classification, and localization.

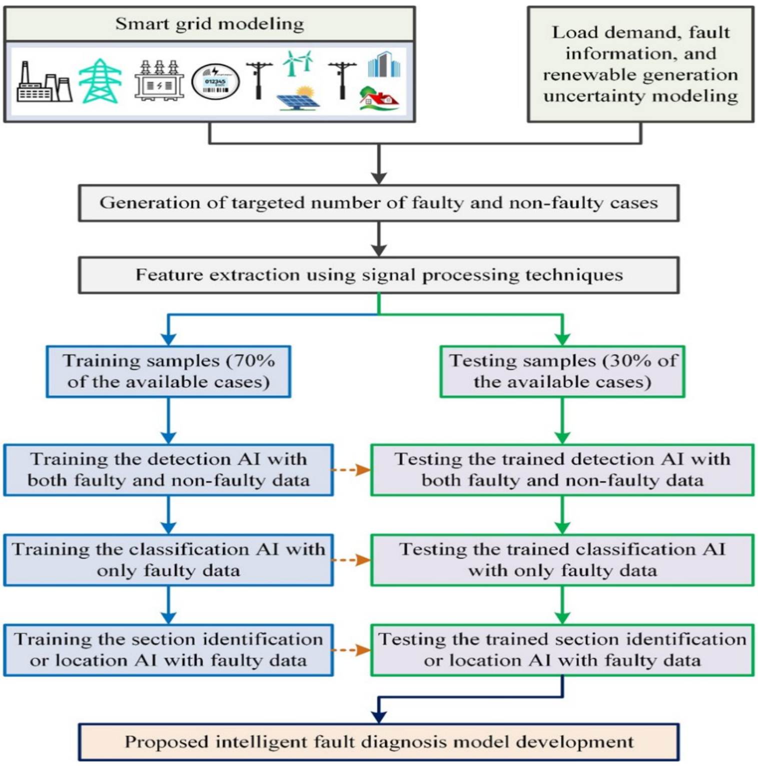

Fig. 3. Unified fault diagnosis framework.

3.4.1. Fault Modeling

The distribution network model was built in MATLAB/Simulink. Seven fault types from [4] were simulated, single-line-to-ground (AG, BG, CG), double-line-to-ground (ABG, ACG, BCG), and three-phase-to-ground (ABCG). Fault resistance (R_f) was randomized between 0.5 and 15 Ω, and a ±5% load variation was applied to emulate different operating conditions. Along the 12 km feeder, faults were imposed every 0.25 km from 0.25 km to 11.75 km; for each location, 15 scenarios with varying fault and load conditions were generated, yielding 705 cases per fault type. For each case, two cycles (one pre-fault and one post-fault) were captured at the sending end, and the same at the receiving end, providing two current measurements at two distinct locations.

Non-faulty (NF) data generation: To make a balanced data set to detect and classify, as many non-faulty conditions as possible were created by simulating the identical feeder in the normal operation (no fault applied). In NF run, the load demand (P/Q setpoints with variation of +5% to -5% load demand) and the PV farm output (60% to 100% rated power) were varied to give the operating point that reflected realistic grid uncertainty. At the receiving end and sending end of each NF scenario three-phase currents were measured with the same sampling rate and same window length as in fault cases (two cycles).

Labels: NF samples are labeled "Not Faulty" for the detector, and assigned to the eighth class (NF) for the classifier, while faulted samples are labeled by fault type (AG, BG, CG, ABG, ACG, BCG, ABCG).

3.4.2. Feature Extraction

Two signal processing techniques were implemented in this paper for feature extraction. Feature extraction from the STFT was carried out by computing statistical indices of the STFT matrices corresponding to faulted signals. Prior work [43] commonly uses features such as amplitude, amplitude slope, fault onset time, energy, mean, and standard deviation (SD). Following the practice in [44, 45], we focused on mean, SD, maximum frequency, and maximum magnitude. Our implementation for STFT and HHT follows the same signal-processing strategy and parameterization as in our previously published studies [24, 46]. Specifically, the extracted features are:

1) Mean of the column-wise maxima of the STFT matrix.
2) The frequency value associated with the global maximum amplitude in the matrix.
3) SD of the phase values at the column-wise peak-magnitude values.
4) SD of the entries at the row-wise peak-magnitude values.
5) SD of the entries at the column-wise peak-magnitude values.
6) Energy of the entries corresponding to each column's peak-magnitude value.

Energy has been calculated using the equation:

$$E_n = \sum_{k=M_1}^{M_2} |S(n,k)|^2 \tag{16}$$

where $S(n,k)$ is the sampling point in the S matrix at the n^{th} row and k^{th} column. Moreover, M_1 and M_2 represent the starting and ending columns, respectively, for the desired sub-matrix (8193 × 2292 matrix) to compute the critical energy features accordingly.

Each STFT yields 17 entries. The first two feature groups (mean and peak-frequency) contribute 2×17 = 34 values per phase, or 34×3 = 102 across the three phases. The remaining four features add 4 values per phase, giving 4×3 = 12 more. Thus, each measurement location provides 102 + 12 = 114 features; with currents recorded at two nodes, this becomes 114×2 = 228.

Furthermore, HHT extracted many IMFs from the recorded three-phase currents. Due to the variability of the number of IMFs generated, the last 3 IMFs were passed to the HT. Thus, 3 IAs and 3 IFs were generated by the HT for each phase. Afterward, six statistical indices (mean, standard deviation, maximum value, variance, energy, and kurtosis) of the IAs were computed after they had been generated. Similarly, the IFs' variance and average were computed. The indicated indices were based on the works of [47], [48], [49] in which an investigation of power quality disturbance situations was conducted. Moreover, the total number of IMFs generated was added to the above features. Therefore, 25 features in total are extracted per phase, meaning that 75 features are generated for the three phases. Since the three-phase currents are measured at two nodes, then two measurements are obtained, and hence, a total of 150 features is generated.

3.4.3. Fault Diagnosis Model

All extracted features form the dataset used to train and evaluate FFNN models for fault detection, classification, and localization. To assess robustness to training-set size, several train/test splits were tried initially, then the split was fixed at 70% for training and 30% for testing to compare performance metrics. The detection model shown in Fig. 4 is a binary classifier that labels signals as faulty or non-faulty. The classification model shown in Fig. 5 assigns faults to one of seven types, with an eighth output indicating no fault. Furthermore, the localization model shown in Fig. 6 is a regression network with a single output neuron that predicts the fault location.

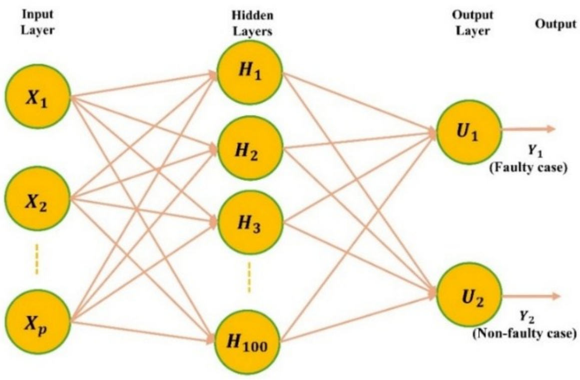

Fig. 4. Neural network used for fault detection (binary classification), the input dimensionality is p=228 with STFT features and p=150 with HHT features.

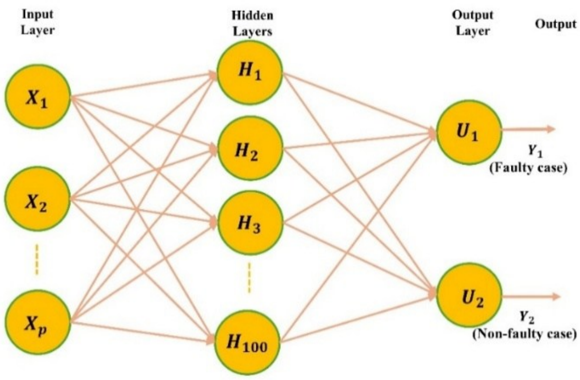

Fig. 5. Neural network utilized for fault type classification, the input dimensionality is p=228 with STFT features and p=150 with HHT features.

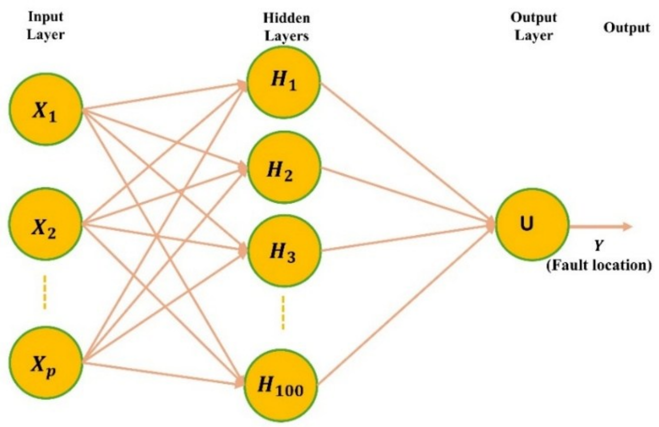

Fig. 6. Neural network utilized for fault localization, the input dimensionality is p=228 with STFT features and p=150 with HHT features.

4. RESULTS AND DISCUSSIONS

This section presents results obtained by pairing both signal-processing techniques with feed-forward neural networks to diagnose faults in the active distribution feeder. Although the STFT-based feature set is high dimensional, it is during offline training that the computational load is mainly encountered. Besides that, the learning algorithm implicitly deals with feature redundancy and there was no degradation in classification performance. For detection and classification, the dataset comprises 4,935 faulty cases (705 samples for each of the seven fault types) and 4,935 non-faulty cases. Three-phase currents were measured at two nodes, and features were extracted, 150 using HHT and 228 using STFT. The data were then cleaned, analyzed, and split into training and testing sets to build the fault-detection, fault-classification, and fault-localization models. It is worth noting that the features of HHT and STFT have been separated so that models trained with HHT features can be compared in performance with those based on STFT features. In addition, FFNN models with various optimizers and activation functions were fine-tuned and determined, as shown in Table 2, to achieve reasonable data generalization and best performance.

In order to have a fair comparison, HHT and STFT features were treated as distinct inputs, i.e. models trained with HHT were trained and tested with HHT features only, and same case with STFT. Table 2 comprises the full FFNN architectures and training environments of each model. To prevent train test leakage, the dataset split was done at preprocessing and feature normalization (z-score scaling) was calculated using only the training set and then applied to the test set without any modifications to either guarantee that the test set was not in any way used during preprocessing or training.

In the first experiment, the detection and classification accuracy were measured for STFT and HHT models. To study sensitivity to training-set size, we varied the test fraction f_{test} (percentage of the total dataset reserved for testing) from 5% to 95%. For each f_{test}, the remaining $1- f_{test}$ portion was used for training. Unless otherwise stated, the final comparison tables use f_{test} =30% (70/30 split). To perform detection and classification, we applied a random train/test split, due to the balanced nature of the dataset (equal faulty and non-faulty samples and uniform sampling of fault types), the splits have similar class distributions. To ensure localization, we also employed random split, and we ensured that the sample of fault-location (created at 0.25 km each along the feeder) appears in both training and testing sets. As shown in Fig. 7, HHT outperformed STFT with an accuracy of almost 100% for most of the various training data availabilities. However, it can be concluded from Fig. 8 that STFT outperformed HHT for fault classification with very high accuracy (more than 98%) even when minimum training data (5%) was provided. In contrast, the HHT-based model's accuracy was drastically reduced to 89% when training data was reduced. This demonstrates the robustness of the STFT-based model for fault classification in the presence of less training data available.

To provide class-wise insight beyond overall accuracy, we additionally report confusion matrices and per-class precision, recall, and F1-score for both the detector and the 8-class classifier. Tables 3-4 present the confusion matrices of the STFT and HHT based fault detectors on the test set, showing correct detections. Tables 5-6 report the corresponding per-class precision, recall, and F1-score, providing class-wise insight and highlighting any bias toward faulty or non-faulty classes.

Table 2. Hyper-parameters of the utilized neural networks.

Model	Feature set	Hidden layers (neurons)	Hidden activation	Output layer	Loss function	Opti.	Learning rate	Batch size	Max iter. (epochs)	Weight init.	Regularization	Random seeds	Normalization & leakage prevention
Detector (binary: Faulty vs NF)	STFT; HHT	1 (100)	ReLU	1 unit (binary); internal sigmoid mapping (sklearn)	Log-loss (binary cross-entropy)	Adam	constant; learning_rate_init = 0.001	auto (sklearn)	200 (set explicitly)	Glorot/Xavier uniform (sklearn default)	L2 (weight decay); alpha = 0.0001; no dropout	Split: random_state=4; MLP: random_state=1	StandardScaler (z-score) fit on TRAIN only; applied to TEST. Split performed before scaling.
Classifier (8-class: NF + 7 faults)	STFT; HHT	1 (100)	ReLU	8 units (multiclass); internal softmax mapping (sklearn)	Log-loss (categorical cross-entropy)	Adam	constant; learning_rate_init = 0.001	auto (sklearn)	5000 (to ensure convergence)	Glorot/Xavier uniform (sklearn default)	L2 (weight decay); alpha = 0.0001; no dropout	Split: random_state=4; MLP: random_state=1	StandardScaler (z-score) fit on TRAIN only; applied to TEST. Split performed before scaling.
Localizer (regression: fault location)	STFT (tuned); HHT (optional tuned)	STFT: 3 (500, 500, 200); HHT: 4 (500, 500, 500, 500)	ReLU	1 unit, linear output (sklearn regressor)	Squared error (MSE)	Adam	constant; learning_rate_init = 0.001	auto (sklearn)	STFT: 10000; HHT: 10000	Glorot/Xavier uniform (sklearn default)	L2 (weight decay); alpha = 0.0001; no dropout	Split: random_state=4; MLP: random_state=3	MinMaxScaler fit on TRAIN only; applied to VAL/TEST. (Optional) y scaling to [0,1] if used. Split performed before scaling.

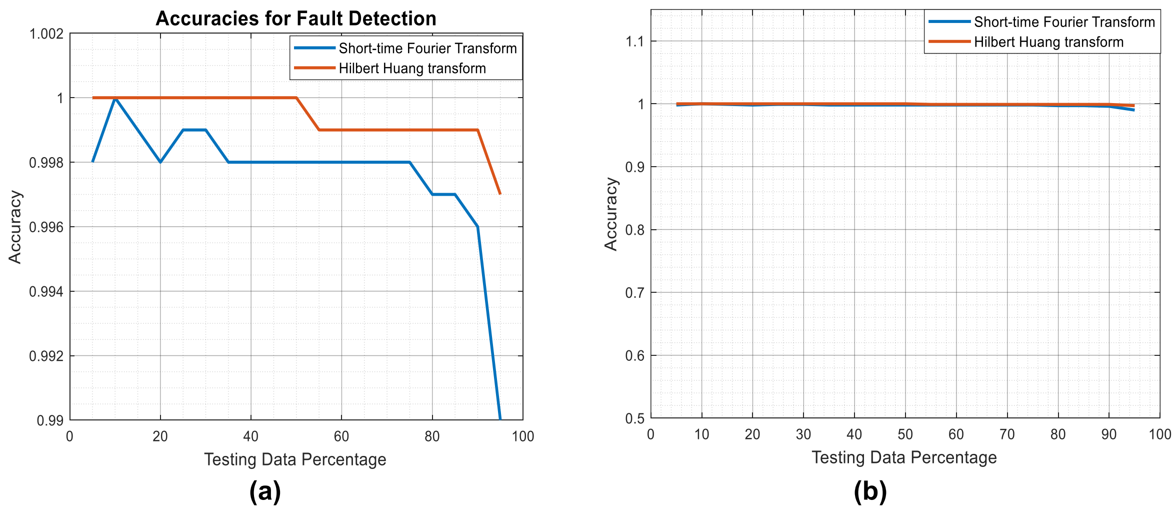

Fig. 7. Comparing the accuracies of HHT and STFT models for fault detection in various training size scenarios.

Tables 7–8 present the confusion matrices of the STFT and HHT based 8-class fault classifiers (AG, BG, CG, ABG, ACG, BCG, ABCG, and NF), which reveal the specific fault categories that are occasionally confused. Tables 9–10 report the corresponding per-class precision, recall, and F1-scores, providing a detailed class-wise assessment. Notably, the NF class is perfectly identified in both methods, while the few misclassifications for HHT occur only among fault classes with similar signatures.

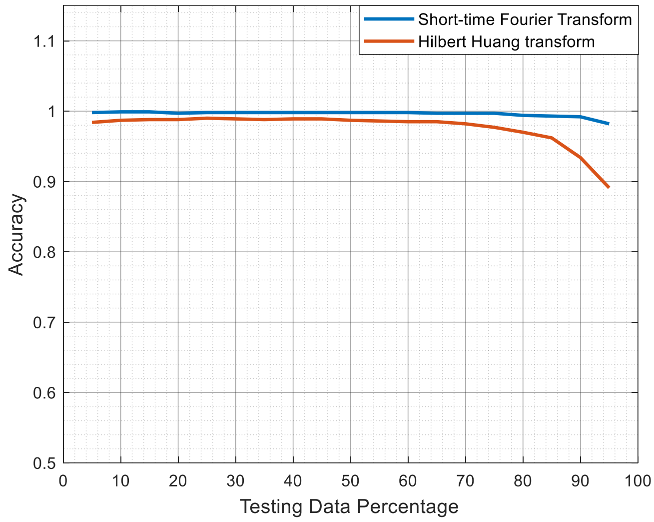

Fig. 8. Comparing the accuracies of HHT and STFT models for fault classification in various training size scenarios.

Table 3. Detector (STFT) confusion matrix (accuracy = 0.9997).

True \ Pred	NonFaulty	Faulty
NonFaulty	1498	0
Faulty	1	1462

Table 4. Detector (HHT) confusion matrix (accuracy = 1.0000).

True \ Pred	NonFaulty	Faulty
NonFaulty	1484	0
Faulty	0	1477

Table 5. Detector (STFT) Per-class precision/recall/F1.

Class	Precision	Recall	F1	Support
NonFaulty	0.99933	1.00000	0.99967	1498
Faulty	1.00000	0.99932	0.99966	1463

Table 6. Detector (HHT) Per-class precision/recall/F1.

Class	Precision	Recall	F1	Support
NonFaulty	1.00000	1.00000	1.00000	1484
Faulty	1.00000	1.00000	1.00000	1477

Table 7. Classifier (STFT) confusion matrix (accuracy = 0.9997).

True \ Pred	AG	BG	CG	ABG	ACG	BCG	ABCG	NF
AG	199	0	0	0	0	0	0	0
BG	0	206	0	0	0	0	0	0
CG	0	0	209	0	0	0	0	0
ABG	0	0	0	215	0	0	0	0
ACG	0	1	0	0	222	0	0	0
BCG	0	0	0	0	0	207	0	0
ABCG	0	0	0	0	0	0	204	0
NF	0	0	0	0	0	0	0	1498

Table 8. Classifier (HHT) confusion matrix (accuracy = 0.9963).

True \ Pred	AG	BG	CG	ABG	ACG	BCG	ABCG	NF
AG	221	1	0	0	0	0	0	0
BG	0	188	0	2	0	1	0	0
CG	0	0	228	0	0	0	0	0
ABG	0	0	0	206	0	0	1	0
ACG	0	0	0	0	205	2	1	0
BCG	0	0	0	1	0	216	0	0
ABCG	0	0	0	1	0	1	202	0
NF	0	0	0	0	0	0	0	1484

Table 9. Classifier (STFT) Per-class precision/recall/F1.

Class	Precision	Recall	F1	Support
AG	1.00000	1.00000	1.00000	199
BG	0.99517	1.00000	0.99758	206
CG	1.00000	1.00000	1.00000	209
ABG	1.00000	1.00000	1.00000	215
ACG	1.00000	0.99552	0.99775	223
BCG	1.00000	1.00000	1.00000	207
ABCG	1.00000	1.00000	1.00000	204
NF	1.00000	1.00000	1.00000	1498

Table 10. Classifier (HHT) per-class precision/recall/F1.

Class	Precision	Recall	F1	Support
AG	1.00000	0.99550	0.99774	222
BG	0.99471	0.98429	0.98947	191
CG	1.00000	1.00000	1.00000	228
ABG	0.98095	0.99517	0.98801	207
ACG	1.00000	0.98558	0.99274	208
BCG	0.98182	0.99539	0.98856	217
ABCG	0.99020	0.99020	0.99020	204
NF	1.00000	1.00000	1.00000	1484

In addition to average localization metrics, we report the distribution of localization errors over the test set. Figure 9 shows the empirical CDF and boxplot of the absolute error, for the STFT- and HHT-based localizers, while Table 11 summarizes MAE, RMSE, median |e|, and the 90th-percentile. Since fault location is physically bounded by the feeder length, predicted locations were constrained to the feasible range [0.25,11.75] km before computing localization errors.

Table 11. Localization error summary statistics on the test set (70/30 split; clipped predictions)

Method	MAE [km]	RMSE [km]	Median |e| [km]	90th percentile |e| [km]
STFT	1.0599	1.4750	0.8222	2.2045
HHT	1.8664	2.7164	1.2451	4.3735

To evaluate robustness under uncertainty in fault parameters and operating conditions, localization error versus fault resistance and PV operating level are analyzed. Test samples were grouped into bins, and the absolute localization error was summarized per bin using MAE and the 90th-percentile error. Tables 12 and 13 report the resulting sensitivity trends in terms of MAE and 90th-percentile error.

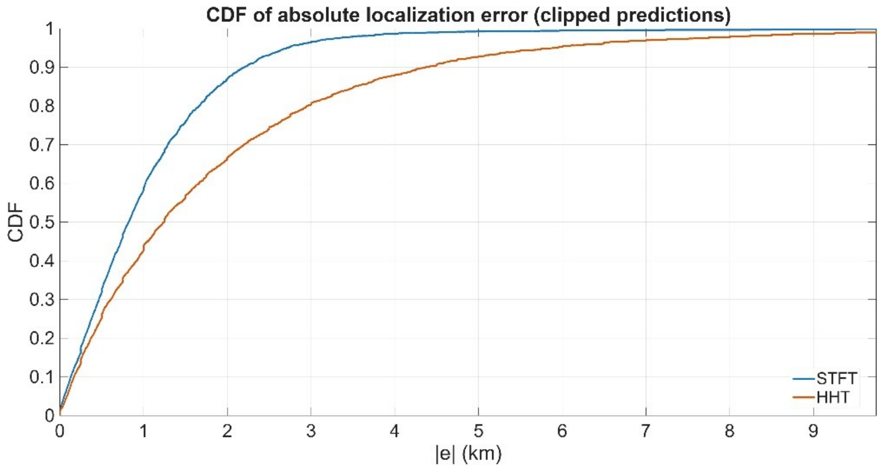

(a)

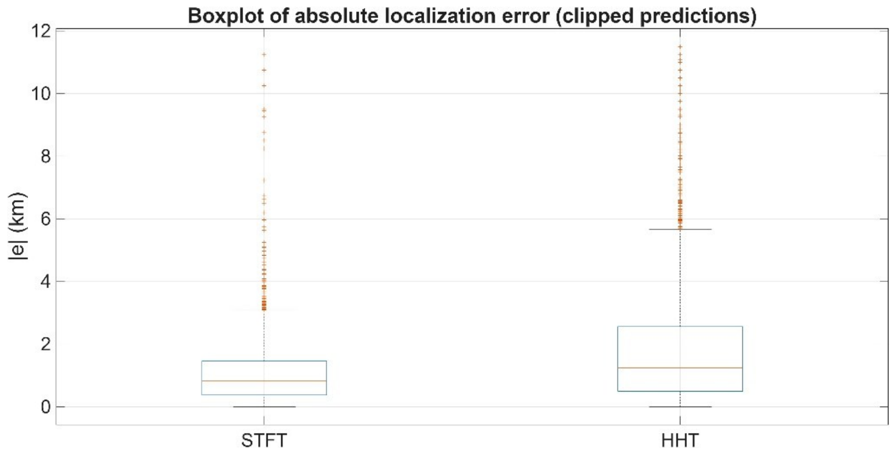

(b)

Fig. 9 a) CDF and; b) boxplot of absolute localization error (clipped predictions) – STFT vs HHT.

Table 12. Sensitivity of localization error (test set) to fault resistance.

Fault resistance bin R_f [Ω]	N	MAE [km]	90th percentile |e| [km]
0.5–2	170	0.98755	1.9587
2–8	581	1.0186	2.1493
8–15	712	1.0453	2.2566

Table 12 shows that localization accuracy degrades only slightly as R_f increases, indicating that the proposed localizer remains robust even for higher-resistance faults.

Table 13. Sensitivity of localization error (test set) to PV operating level (normalized).

PV level bin [% rated]	N	MAE [km]	90th percentile |e| [km]
60–75%	160	0.92080	1.9162
75–90%	182	0.92571	2.4699
90–100%	153	1.11000	2.3751

Table 13 summarizes localization performance under varying PV operating levels (normalized operating index), showing comparable MAE/P90 across bins and therefore limited sensitivity to operating-point variation.

To provide a contextual benchmark beyond the internal comparison of STFT and HHT, Table 14 summarizes representative published approaches and their reported performance. As these studies employ different feeders, measurement setups, and evaluation protocols, the comparison is intended as a performance benchmark rather than a strict head-to-head comparison.

Table 14. Comparison with representative published baselines.

Work	Method / Features	Task(s)	#Classes	Reported metric(s)	Key reported performance
[50]	Raw currents + CNN hierarchy	Fault type + section ID + exact location	8 / 8 / reg.	Accuracy; location error	Fault classification Acc = 99.46%; section ID Acc ≈ 99.38%; location error ≈ 0.9%
[24]	S-Transform features + FFNN	Detection + Classification	2 / 7	Accuracy	Overall classification Acc = 99.93%; detection reported as 100%
[45]	HHT/DWT-based FFNN (reported)	Detection/Classification/Localization (reported)	–	Accuracy (noise-free)	Reported classification accuracy > 99.00% (noise-free)
[51]	WT features → RGB + GoogLeNet; CNN for location	Identification + Classification + Location	10 (fault states)	Accuracy; average location error	Validation accuracy reported up to 100% (example); average location error ≈ 0.215 km
[52]	DWT (db5, level-1) + PCA + feed-forward DNN	Fault location (transmission line)	reg.	MAE; MSE	Reported MAE ≈ 0.0180–0.0254 and MSE ≈ 5.0089e−04–0.0011 (by fault type)
This work (STFT+FFNN)	STFT features + FFNN	Detection + Classification + Localization	2 / 8 / reg.	Acc; per-class P/R/F1; MAE/P90	Detector Acc = 99.97%; 8-class Acc = 99.97%
This work (HHT+FFNN)	HHT features + FFNN	Detection + Classification + Localization	2 / 8 / reg.	Acc; per-class P/R/F1; MAE/P90	Detector Acc = 100.00%; 8-class Acc = 99.63%

The FFNN was configured as a regression model to estimate fault location. Robustness was evaluated using the coefficient of determination (R^2), mean absolute error (MAE), and root mean squared error (RMSE).

Smaller MAE and RMSE indicate better predictive accuracy, while $R^2 \epsilon$ [0,1] measures goodness of fit, with $R^2 = 1$ denoting a perfect prediction and $R^2 = 0$ indicating that the model fails to identify relationships among the dependent and independent variables, thus generating inaccurate results. To assess sensitivity and performance, we varied the amount of training data for both STFT- and HHT-based feature sets, using RMSE as the primary metric for comparison. As can be seen in Table 15 and Table 16, the STFT-based localization model outperformed the HHT-based model by achieving higher R^2 values in all fault types, demonstrating the robustness of the STFT model in localizing faults in the network.

Table 15. Performance metrics for STFT fault localization model using 70% training and 30% testing data.

Fault type	R^2	RMSE [km]	MAE [km]
ABCG	0.986	0.381	0.193
ABG	0.994	0.243	0.172
ACG	0.993	0.262	0.153
BCG	0.997	0.177	0.128
AG	0.994	0.245	0.161
BG	0.996	0.197	0.143
CG	0.995	0.241	0.171

Table 16. Performance metrics for the HHT fault localization model using 70% training and 30% testing data.

Fault type	R^2	RMSE [km]	MAE [km]
ABCG	0.974	0.531	0.335
ABG	0.981	0.453	0.324
ACG	0.976	0.514	0.365
BCG	0.973	0.537	0.365
AG	0.977	0.503	0.349
BG	0.967	0.600	0.380
CG	0.985	0.398	0.300

Moreover, another experiment was conducted by combining all the fault types into one dataset and feeding it to the STFT and HHT-based fault localization models. This means models independent of fault type (i.e., without prior fault classification) will be evaluated. As can be seen in Fig. 10, when the percentage of testing data of the total data varied between 5% to 95%, both models' performance degraded when more data was set for testing since fewer training examples were provided. However, it can be noticed that the STFT-based model again outperformed the HHT-based model since its RMSE values were less than their corresponding values for the HHT model for almost all scenarios. Moreover, Fig. 11 compares the R^2 values between the two models with the same conditions to investigate their performance further. It can be seen that R^2 for the STFT model remained higher than its corresponding value in the HHT model for most of the cases, except for the extreme scenarios where more than 75% of the data was set as testing data, therefore showing that a reliable fault localization with very high certainty can be obtained by the STFT-based model given a reasonable amount of data. This, combined with results from Fig. 10, shows the effectiveness of STFT-based models in localizing faults with various scenarios of training data availability.

Furthermore, another experiment compared the HHT and STFT-based models. In this experiment, the training data was fixed to 70% of the total data, while the remaining was set for testing the models. The results in Table 17 demonstrate that when enough training data is fed to the models, the STFT outperformed HHT for all three-performance metrics. This, combined with the previous experiment results, demonstrates the robustness of the STFT-based model over the HHT-based model in fault localization, even in the absence of providing fault type as a feature, thus eliminating the need for prior fault classification.

To thoroughly test the proposed models in actual scenarios and inspect the results, 15 random faults have been selected and fed to the pre-trained detection, classification, and localization models shown earlier. Table 18 shows the actual locations of the samples compared to the predicted location by the developed model. The small error in the predictions shows the generalizability of the localization models and their adequate performance when used to predict future faults. Further, Table 19 shows 10 faults with their correct fault type compared to the predictions of the developed classification models proposed earlier. As can be seen, most of these test cases have been identified correctly by the classifiers, with the STFT-based classifier performing better in this scenario. Additionally, Table 20 shows another 10 faults when the binary is classified as faulty or non-faulty. The detection models trained earlier have been again tested on this sample to show the performance, which proved the validity of the detection models.

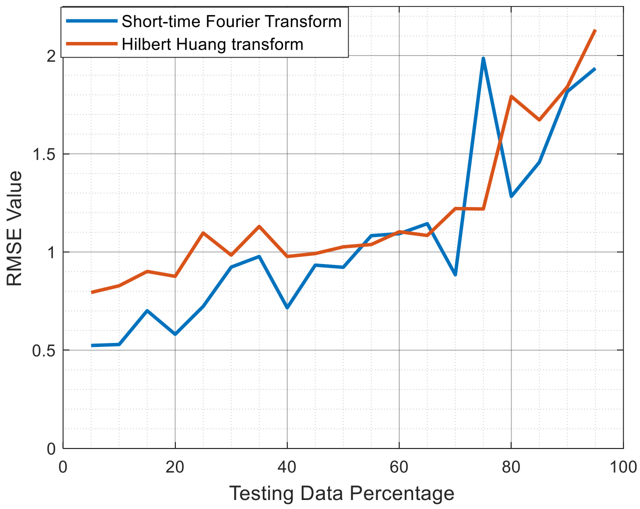

Fig. 10. A comparison of RMSE between STFT and HHT models for fault localization with no prior fault classification.

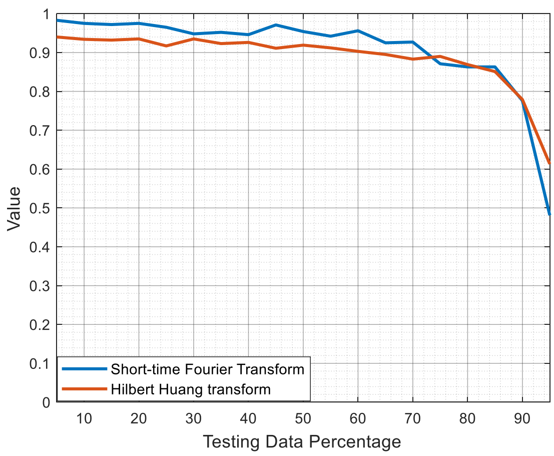

Fig. 11. Comparing R^2 values between STFT and HHT models for fault localization without prior fault classification.

Table 17. Comparing STFT and HHT fault localization models for the dataset of combined fault types and 70% training data.

Technique	Short-time Fourier transform	Hilbert Huang transform
R^2	0.988	0.948
RMSE [km]	0.365	0.769
MAE [km]	0.226	0.535

Table 18. Comparing STFT and HHT fault localization models performance in randomly selected samples.

Sample Number	HHT-based Localizer		STFT-based Localizer	
	Actual Location	Predicted Location	Actual Location	Predicted Location
1	4.00	4.5	11.00	11.25
2	4.25	4.8	2.00	1.55
3	8.00	8.26	10.75	10.83
4	9.00	9.16	8.25	8.17
5	9.00	8.09	9.00	9.47
6	2.50	3.44	4.00	3.47
7	7.50	7.59	8.25	8.68
8	11.25	11.40	2.50	2.63
9	2.25	3.15	7.75	7.86
10	4.25	5.12	0.75	0.56
11	7.25	7.20	6.00	5.95
12	0.75	0.56	0.25	1.28
13	3.25	4.49	4.50	4.09
14	2.00	2.50	11.25	11.02
15	10.75	10.76	6.25	5.94

Table 19. Comparing STFT and HHT fault classification models performance in randomly selected samples.

Sample Number	True Fault Type	HHT-based Classifier	STFT-based Classifier
1	AG	AG	AG
2	ABG	ABG	ABG
3	CG	CG	CG
4	BG	CG	BG
5	NF	NF	NF
6	ABCG	ABCG	ABCG
7	NF	NF	NF
8	ABCG	ABCG	ABCG
9	CG	CG	CG
10	NF	NF	NF

Table 20. Comparing STFT and HHT fault detection models performance in randomly selected samples.

Sample Number	Truth	HHT-based Detector	STFT-based Detector
1	Faulty	Faulty	Faulty
2	Faulty	Faulty	Faulty
3	Faulty	Faulty	Faulty
4	Faulty	Faulty	Faulty
5	Not Faulty	Not Faulty	Not Faulty
6	Faulty	Faulty	Faulty
7	Faulty	Faulty	Faulty
8	Not Faulty	Not Faulty	Not Faulty
9	Not Faulty	Not Faulty	Not Faulty
10	Faulty	Faulty	Faulty

5. CONCLUSIONS AND FUTURE WORK

This study introduced a unified protocol for diagnosing and locating faults in active distribution feeders to improve supply reliability and effectiveness. The approach fuses HHT- and STFT-derived features with FFNNs, which successfully detected, classified, and localized faults in a simulated network. In the HHT pipeline, measured currents were decomposed into IMFs via EMD, the last three IMFs were then processed with the Hilbert transform to obtain instantaneous amplitude and frequency. Statistical metrics of these IA/IF signals were computed and used as features. Moreover, the STFT was employed for fault diagnosis using statistical indices calculated from its resulting spectra as extracted features. The features mentioned above were then utilized as inputs to train the FFNN, enabling the development of robust fault diagnostic algorithms. The results confirmed the reliability and effectiveness of the proposed models. The STFT-based model outperformed in fault classification and localization, while the HHT-based model excelled in fault detection. Notably, the fault localization model demonstrated outstanding accuracy without dependence on prior fault classification, enabling a fast and precise fault localization process. Moreover, the developed models showcased their ability to handle various load conditions, uncertainty in renewable energy generation, and ambiguity in fault information. The proposed methodology holds great promise and should be further validated through experimental applications in real-world active distribution networks. Such validaftion would provide empirical evidence of the efficacy of the proposed approach, leading to significant benefits for the power systems industry. The presented framework is validated using simulated data on a modeled feeder; therefore, conclusions are limited to the tested scenario and operating envelope. Future work will include additional feeder configurations and topology variations, feature selection, realistic measurement noise, and experimental/field validation, along with real-time hardware implementation.

Acknowledgement: The authors gratefully acknowledge the research support provided by the IRC for Sustainable Energy Systems at King Fahd University of Petroleum & Minerals (KFUPM) through project no. INSE2632.

REFERENCES

[1] T. Zhihai *et al.*, "An accurate fault location method of smart distribution network," China International Conference on Electricity Distribution, 2014, doi: 10.1109/CICED.2014.6991842.

[2] R. Kumar, D. Saxena, "Fault location in multilateral distribution network with electric vehicle charging load," *Energy Storage*, vol. 1, no. 5, 2019, doi: 10.1002/est2.85.

[3] S. Jamali, A. Bahmanyar, "A new fault location method for distribution networks using sparse measurements," *International Journal of Electrical Power & Energy Systems*, vol. 81, pp. 459–468, 2016, doi: 10.1016/j.ijepes.2016.02.046.

[4] S. Gururajapathy, H. Mokhlis, H. Illias, "Fault location and detection techniques in power distribution systems with distributed generation: a review," *Renewable and Sustainable Energy Reviews*, vol. 74, pp. 949–958, 2017, doi: 10.1016/j.rser.2017.03.021.

[5] S. Mou, N. Yang, H. Chen, Z. Liu, S. Yang, "A new fault location method for modern distribution network based on system parameters estimation and self-correction," 8th International Conference on Smart Grid and Smart Cities, 2024, doi: 10.1109/ICSGSC62639.2024.10813814.

[6] Z. Huang, "Optimization of distribution network fault restoration strategy based on fuzzy logic algorithm," *Engineering Research Express*, vol. 7, no. 3, p. 035325, 2025, doi: 10.1088/2631-8695/adef95.

[7] T. Lu, S. Hou, "Fault location algorithm for distribution network with distributed generation based on domain-adaptive TGATv2," *IET Generation, Transmission and Distribution*, vol. 19, no. 1, 2025, doi: 10.1049/gtd2.70033.

[8] W. Xu, J. Li, L. Yang, Q. Yu, "Faults locating of power distribution systems based on successive PSO-GA algorithm," *Scientific Reports*, vol. 14, no. 1, 2024, doi: 10.1038/s41598-024-61306-w.

[9] A. Bretas, R. Salim, "A new fault location technique for distribution feeders with distributed generation," *WSEAS Transactions on Power Systems*, vol. 1, no. 5, pp. 894–900, 2006.

[10] J. Wen, X. Qu, J. Liu, S. Lin, Q. Xiao, "A novel fault location method for the active distribution network based on dynamic quantum genetic algorithm," *Electrical Engineering*, vol. 106, no. 4, pp. 4719–4735, 2024, doi: 10.1007/s00202-024-02244-8.

[11] Z. Zhou, Y. Wen, M. Deng, J. Ma, J. Zeng, X. She, "Fault location method for new distribution networks based on waveform matching of time–frequency travelling waves," *IET Smart Grid*, vol. 7, no. 6, pp. 929–939, 2024, doi: 10.1049/stg2.12190.

[12] H. Yang, X. Liu, Y. Guo, P. Zhang, "Fault location of active distribution networks based on the golden section method," *Mathematical Problems in Engineering,* vol. 2020, pp. 1–9, 2020, doi: 10.1155/2020/6937319.

[13] K. Jiang, H. Wang, M. Shahidehpour, B. He, "Block-sparse bayesian learning method for fault location in active distribution networks with limited synchronized measurements," *IEEE Transactions on Power Systems*, vol. 36, no. 4, pp. 3189–3203, 2021, doi: 10.1109/TPWRS.2021.3049443.

[14] S. Lin, Z. Y. He, X. P. Li, Q. Qian, "Travelling wave time–frequency characteristic-based fault location method for transmission lines," *IET Generation, Transmission & Distribution*, vol. 6, no. 8, p. 764, 2012, doi: 10.1049/iet-gtd.2011.0703.

[15] A. Fedorov, V. Petrov, O. Afanasieva, I. Zlobina, "Limitations of traveling wave fault location," Ural Smart Energy Conference, 2020, doi: 10.1109/USEC50097.2020.9281153.

[16] P. Relaying, "IEEE Guide for Determining Fault Location on AC Transmission and Distribution Lines,'' Sponsored by the Power System Relaying Committee IEEE Power and Energy Society, 2005, doi: 10.1109/IEEESTD.2005.96207.

[17] E. Reche, J. Sousa, D. Coury, R. Fernandes, "Data mining-based method to reduce multiple estimation for fault location in radial distribution systems," *IEEE Transactions Smart Grid*, vol. 10, no. 4, pp. 3612–3619, 2019, doi: 10.1109/TSG.2018.2832840.

[18] L. Acacio, P. Guaracy, T. Diniz, D. Araujo, L. Araujo, "Evaluation of the impact of different neural network structure and data input on fault detection," IEEE PES Innovative Smart Grid Technologies, 2017, doi: 10.1109/ISGT-LA.2017.8126699.

[19] M. Ijaz, M. Shafiullah, M. Abido, "Classification of power quality disturbances using Wavelet Transform and Optimized ANN," 18th International Conference on Intelligent System Application to Power Systems, 2015, doi: 10.1109/ISAP.2015.7325522.

[20] M. Rodriguez, J. Sotomonte, J. Cifuentes, M. Bueno-Lopez, "Classification of power quality disturbances using hilbert huang transform and a multilayer perceptron neural network model," International Conference on Smart Energy Systems and Technologies, 2019, doi: 10.1109/SEST.2019.8849114.

[21] S. Swain, B. Subudhi, "Grid SYNCHRonization of a PV system with power quality disturbances using unscented kalman filtering," *IEEE Transactions on Sustainable Energy*, vol. 10, no. 3, pp. 1240–1247, 2019, doi: 10.1109/TSTE.2018.2864822.

[22] M. Shafiullah, M. Khan, S. Ahmed, "PQ disturbance detection and classification combining advanced signal processing and machine learning tools," *Power Quality in Modern Power Systems*, 2021, doi: 10.1016/B978-0-12-823346-7.00012-8.

[23] K. Moloi, A. Yusuff, "power distribution system fault diagnostic using genetic algorithm and neural network," Southern African Universities Power Engineering Conference/Robotics and Mechatronics/Pattern Recognition Association of South Africa, 2021, doi: 10.1109/SAUPEC/RobMech/PRASA52254.2021.9377241.

[24] M. Shafiullah, M. Abido, "S-transform based FFNN approach for distribution grids fault detection and classification," *IEEE Access*, vol. 6, pp. 8080–8088, 2018, doi: 10.1109/ACCESS.2018.2809045.

[25] H. Lala, S. Karmakar, S. Ganguly, "Detection and localization of faults in smart hybrid distributed generation systems: a stockwell transform and artificial neural network-based approach," *International Transactions on Electrical Energy Systems*, vol. 29, no. 2, p. e2725, 2019, doi: 10.1002/etep.2725.

[26] M. Shafiullah, M. Abido, T. Abdel-Fattah, "Distribution grids fault location employing ST based optimized machine learning approach," *Energies*, vol. 11, no. 9, p. 2328, 2018, doi: 10.3390/en11092328.

[27] M. Guo, N. Yang, W. Chen, "Deep-learning-based fault classification using hilbert–huang transform and convolutional neural network in power distribution systems," *IEEE Sensors Journal,* vol. 19, no. 16, pp. 6905–6913, 2019, doi: 10.1109/JSEN.2019.2913006.

[28] K. Jia, T. Bi, Z. Ren, D. Thomas, M. Sumner, "High frequency impedance based fault location in distribution system with DGs," *IEEE Transactions on Smart Grid*, vol. 9, no. 2, pp. 807–816, 2018, doi: 10.1109/TSG.2016.2566673.

[29] G. Manassero, S. di Santo, L. Souto, "Heuristic method for fault location in distribution feeders with the presence of distributed generation," *IEEE Transactions on Smart Grid*, vol. 8, no. 6, pp. 2849–2858, 2017, doi: 10.1109/TSG.2016.2598487.

[30] J. Marín-Quintero, C. Orozco-Henao, W. Percybrooks, J. Vélez, O. Montoya, W. Gil-González, "Toward an adaptive protection scheme in active distribution networks: Intelligent approach fault detector," *Applied Soft Computing,* vol. 98, p. 106839, 2021, doi: 10.1016/j.asoc.2020.106839.

[31] R. Chen, T. Lin, R. Bi, X. Xu, "Novel strategy for accurate locating of voltage sag sources in smart distribution networks with inverter-interfaced distributed generators," *Energies*, vol. 10, no. 11, p. 1885, 2017, doi: 10.3390/en10111885.

[32] Z. Uddin, A. Ahmad, A. Qamar, M. Altaf, "Recent advances of the signal processing techniques in future smart grids," *Human-centric Computing and Information Sciences*, vol. 8, no. 1, p. 2, 2018, doi: 10.1186/s13673-018-0126-9.

[33] M. Shafiullah, M. Abido, A. Al-Mohammed, "Artificial intelligence techniques," *Power System Fault Diagnosis*, 2022, doi: 10.1016/B978-0-323-88429-7.00007-2.

[34] N. Kehtarnavaz, "Frequency domain processing," *Digital Signal Processing System Design*, 2008, doi: 10.1016/B978-0-12-374490-6.00007-6.

[35] M. Kostov, B. Gegov, M. Atanasovski, M. Petkovski, "Short time Fourier transform for power disturbances analysis," Proceedings of the International Scientific Conference on Information, Communication and Energy Systems and Technologies, 2015.

[36] S. Krishnan, "Advanced analysis of biomedical signals," *Biomedical Signal Analysis for Connected Healthcare*, 2021, doi: 10.1016/B978-0-12-813086-5.00003-7.

[37] N. Huang, "Introduction to the hilbert–huang transform and its related mathematical problems," 2005, doi: 10.1142/9789812703347_0001.

[38] K. Alshumayri, M. Shafiullah, "Distribution grid fault diagnostic employing hilbert-huang transform and neural networks," International Conference on Power Energy Systems and Applications, 2022, doi: 10.1109/ICoPESA54515.2022.9754475.

[39] R. Jalaja, B. Biswal, "Power quality event classification using hilbert huang transform," Proceedings of the International Conference on Frontiers of Intelligent Computing, 2013, doi: 10.1007/978-3-642-35314-7_18.

[40] D. Tien Bui, T. Tuan, H. Klempe, B. Pradhan, I. Revhaug, "Spatial prediction models for shallow landslide hazards: a comparative assessment of the efficacy of support vector machines, artificial neural networks, kernel logistic regression, and logistic model tree," *Landslides*, vol. 13, no. 2, pp. 361–378, 2016, doi: 10.1007/s10346-015-0557-6.

[41] S. Masiur Rahman, A. Khondaker, M. Hossain, Md. Shafiullah, Md. Hasan, "Neurogenetic modeling of energy demand in the United Arab Emirates, Saudi Arabia, and Qatar," *Environmental Progress & Sustainable Energy*, vol. 36, no. 4, pp. 1208–1216, 2017, doi: 10.1002/ep.12558.

[42] M. Rana, M. Shahriar, M. Shafiullah, "Levenberg–Marquardt neural network to estimate UPFC-coordinated PSS parameters to enhance power system stability," *Neural Computing & Applications*, vol. 31, no. 4, pp. 1237–1248, 2019, doi: 10.1007/s00521-017-3156-8.

[43] S. Mishra, C. Bhende, B. Panigrahi, "Detection and classification of power quality disturbances using s-transform and probabilistic neural network," *IEEE Transactions on Power Delivery*, vol. 23, no. 1, pp. 280–287, 2008, doi: 10.1109/TPWRD.2007.911125.

[44] B. Kachhepati, "Application of short time Fourier transform (STFT) in power quality monitoring and event classification," New Mexico State University, New Mexico, 2016.

[45] N. Mohamed, M. Shafiullah, H. Anwar, "Machine learning for fault diagnosis in active distribution networks," IEEE 13th International Conference on System Engineering and Technology, 2023, doi: 10.1109/ICSET59111.2023.10295076.

[46] M. Shafiullah, K. AlShumayri, M. Alam, "Machine learning tools for active distribution grid fault diagnosis," *Advances in Engineering Software*, vol. 173, 2022, doi: 10.1016/j.advengsoft.2022.103279.

[47] R. kapoor, M. Tripathi, "Hilbert Huang transform and type-1 fuzzy based recognition and classification of power signal disturbances," International Conference on Recent Innovations in Electrical, Electronics & Communication Engineering, 2018, pp. 2198–2203. doi: 10.1109/ICRIEECE44171.2018.9009350.

[48] D. Das, T. Chakravorti, P. Dash, "Hilbert huang transform with fuzzy rules for feature selection and classification of power quality disturbances," 4th IEEE Uttar Pradesh Section International Conference on Electrical, Computer and Electronics, 2017, pp. 439–445. doi: 10.1109/UPCON.2017.8251088.

[49] R. Kumar, B. Singh, D. Shahani, "Recognition of single-stage and multiple power quality events using hilbert–huang transform and probabilistic neural network," *Electric Power Components and Systems*, vol. 43, no. 6, pp. 607–619, 2015, doi: 10.1080/15325008.2014.999147.

[50] M. Siddique, M. Shafiullah, S. Mekhilef, H. Pota, M. A. Abido, "Fault classification and location of a PMU-equipped active distribution network using deep convolution neural network (CNN)," *Electric Power Systems Research*, vol. 229, 2024, doi: 10.1016/j.epsr.2024.110178.

[51] N. Bon, L. Dai, "Fault identification, classification, and location on transmission lines using combined machine learning methods," *International Journal of Engineering and Technology Innovation*, vol. 12, no. 2, pp. 91–109, 2022, doi: 10.46604/IJETI.2022.7571.

[52] P. Dhole, S. Patil, A. Khan, "Deep neural network based transmission line fault location algorithm," *International Journal of Intelligent Systems and Applications in Engineering,* vol. 2, no. 4, pp. 1369-1380, 2024.